www.maajournal.com

Mediterranean Archaeology and Archaeometry
Vol. 23, No 2, (2023), pp. 1-22
Open Access. Online & Print.

DOI: 10.5281/zenodo.7870973

ARCHAEOLOGICAL BRICKS AND TILES FROM SOUTHEAST BULGARIA- DETERMINATION OF RAW MATERIAL AND PRODUCTION TECHNOLOGY BY CHEMICAL, PHASE, AND THERMAL ANALYSES

Bilyana Kostova*[1], Boyan Dumanov[2] and Katerina Mihaylova[1,3]

[1]New Bulgarian University, Department of Natural Sciences, 21 Montevideo Blvd., 1618 Sofia, Bulgaria
[2]New Bulgarian University, Department of Archaeology, 21 Montevideo Blvd., 1618 Sofia, Bulgaria
[3]Institute of Mineralogy and Crystallography "Akad. I. Kostov", Bulgarian Academy of Sciences, Acad. G. Bonchev Str., bldg.107, 1113 Sofia, Bulgaria

Received: 13/04/2023
Accepted: 27/04/2023
**Corresponding author: Bilyana Kostova (bkostova@nbu.bg)*

ABSTRACT

This work deals with Roman and Late Antique bricks and roof tiles from eight archaeological sites in Southeast Bulgaria. The samples' study was through X-ray fluorescence, powder X-ray diffraction, Fourier transform infrared, and thermal analysis, supported by macro and micro observations. The results indicate the successful combination of the experimental methods to determine with great accuracy the mineral composition and type of the raw clay (regarding the content of carbonate phases), the firing technology, and some findings of high ceramic quality and durability over time. This work shows that the clay type (calcareous type - carbonate-rich clay or non-calcareous type - carbonate-poor clay) cannot be determined by using chemical analysis only. The clay type determination is only possible by combination with thermal analysis in the case of ceramic firing below the calcite decarbonation temperature and by taking into account only the CaO amount included in the clay as calcite, which is calculated from the measured mass loss of calcite decarbonation. The results prove that for a more precise determination of the ceramic firing temperature range, it is necessary to use not only the phase composition (mineral-thermometers), but also the structural features of minerals determined by Fourier transform infrared and thermal analyses. The results evidence the use of identical ceramic manufacturing technologies in the entire geographical area during the Roman and Late Antique periods and a clear perspective for future investigation. They also complement the known archaeological background by interpreting people's knowledge continuity from the Roman age to Late Antiquity and giving insight into their economic and cultural life, based on the ceramic experimental investigations.

KEYWORDS: Late Antique and Roman ceramic tiles and bricks, thermal analysis, phase analysis, chemical analysis

1. INTRODUCTION

Ceramic refer to bricks, tiles, pottery, and wall plasters made of clay and water. Its production was simple, low-cost, and continuous during many archeological periods. Thus, ceramic is the most abundant artifact, making it significant for archaeology. Moreover, it's defined as the first composite material manufactured and developed by humans (Goffer, 2007). The ceramic study provides information about the cultural and economic aspects of ancient societies and helps reconstruction and conservation activities, allowing the creation of modern ceramic analogs compatible with the ancient ones (Cultrone et al., 2001; Elert et al., 2003; Cardiano et al., 2004). The classic archaeological ceramic research includes a classification by macroscopic description. Analytical techniques achieve a transition from observation to empirical investigations due to the determination of ceramic production technology by studying the phase composition, raw clay, and firing temperature in the kiln (Peacock, 1970). The first studies of phase composition were petrographic by thin sections, published by Shepard in 1936. Later, powder X-ray diffraction (PXRD) was applied (Neff, 1993, Xanthopoulou et al., 2020). Recently, a commonly used combination is that of chemical analysis, PXRD, Fourier transform infrared spectroscopy (FTIR), and thermal methods, which are also appropriate techniques for determining ceramic manufacturing conditions (Cardiano et al., 2004; Drebushchak et al., 2005; Papadopoulou et al., 2006; Palanivel and Rajesh Kumar, 2009; Ravisankar et al., 2010; Kotryová et al., 2016; Kılıç et al., 2017; Yan et al., 2021). For ceramic firing temperature determination, a new non-destructive method by electron probe microanalyzer also are indicated in the literature (Baziotis et al., 2020).

In the beginning, ceramic production included three stages - clay paste preparation, forming and shaping into an object (molding), and air drying of the final product. Later, the fourth stage appeared – firing at a minimum of 600°C (Goffer, 2007) up to 950-1050°C (Emami et al., 2016). The quality of the fired ceramic depends on the properties of the raw clay, determined by the clay mineral composition, the production conditions - firing temperature and atmosphere, etc. (Khitab et al., 2021). Clays are sediments or rocks that consist of three mineral groups: clays, accessories, and impurities. The clays are layered silicate minerals separated by similarity in the crystal structure into kaolins, montmorillonites, and illites. Accessory minerals also include layer silicates - micas, chlorites, and vermiculites. The impurities are inorganic (quartz, feldspar, iron minerals, carbonates, gypsum, etc.) and organic phases (Chamley, 1989; Meyers and Speyer, 2003). All clay phases (minerals and organic) show different behavior during firing at different temperatures. Layered silicates (phyllosilicates) containing water undergo dehydration, dehydroxylation, and with prolonged increases in temperature – destruction. Carbonates undergo decarbonation and organic phases – decomposition. At around 950°C occurs: either vitrification with crystallization of a high-temperature phase from the melt or solid-state recrystallization with high-temperature phase formation (Cardiano et al., 2004; El Ouahabi et al., 2015). Which of the two processes takes place depends on the firing atmosphere and the raw clay type - calcareous (carbonate-rich) or non-calcareous (carbonate-poor) (Papadopoulou et al., 2006; Trindade et al., 2009; Badica et al., 2022). All the described thermal processes can be traced in the ceramic artifacts, considering the phyllosilicates' ability to redehydroxylate over time (Hamilton and Hall, 2012).

Generally, the existing studies on ceramic raw material, kiln redox atmosphere, and temperature can be summarized into three groups. Most publications confirm or reject the production of archaeological ceramic from local clay deposits by examining and comparing clay with ceramic artifacts. Some of these works also present clay firing experiments (Drebushchak et al., 2005; Papadopoulou et al., 2006; Trindade et al., 2009; Badica et al., 2022; Aras and Kiliç, 2017). Other publications show only archaeological ceramic studies, mainly determining its firing conditions (Palanivel and Rajesh Kumar, 2009; Krapukaityte et al., 2008; Vlase et al., 2019; Omar, 2022). Fewer publications investigate archaeological ceramic only to determine the type of raw clay and the firing conditions (Cardiano et al., 2004; Bayazit et al., 2014). The latter group of studies is significant for archaeological sites from geographical areas without known clay deposits. Despite many studies, each ceramic is made from a specific raw material and production technology, thus caution is required when extrapolating published results (Cultrone et al., 2001). This requires specific studies for the individual archaeological sites.

This work deals with Roman and Late Antique bricks and roof tiles in order to determine the composition and type of raw clay and the firing technology (kiln temperature and atmosphere) used as well as to specify some characteristics influencing the ceramic quality and durability over time. The sixteen samples studied are from eight archaeological sites with location Sarnena Sredna Gora Mountain and its southern foothills, Southeast Bulgaria. The absence of clay deposits in the geographical area (Kostova et al., 2022) excludes a possible comparison of probable local raw material with the ceramic samples. Achievement of the study goal therefore was accomplished only by studying the chemical and phase composition and

thermal behavior of ceramic samples through chemical analyses (X-ray fluorescence analysis - XRF), structural-phase methods (PXRD and FTIR), and thermal analysis. The performed macro and micro observations of ceramic color and structure assist in the kiln temperature, redox atmosphere, quality, etc. determinations (Bratitsi et al., 2018; Goffer, 2007; Khitab et al., 2021; Gredmaier et al., 2011).

2. MATERIALS AND METHODS

2.1. *Materials*

The study includes sixteen ceramic bricks and roof tiles allocated to the Roman (Fig. 1) and Late Antique (Fig. 2) periods. The sample collection was from eight archaeological sites in Southeast Bulgaria, namely the Sarnena Sredna Gora Mountain and the southern foothills (Fig. 3). Sarnena Sredna Gora Mountain (former Karaca Dağı) is a part of Sredna gora system (Srednogorie). That is a medium-high mountain parallel to the Balkan range but also a specific region of cultural and historical aspects. Karaca Dağı is the ultimate eastern part of Srednogorie, located between the valleys of Srtryma (Westward) and Tundzha rivers (Eastward). In this sense, one might conclude that this mountainous region has been ever in a state of isolation. Still, two passes – the Sveti Nikola in the Bratanski region and Zmeyovo in the Kortenski region intersected the range, thus providing the connection to Sub Balkan valleys and Thrace, and also to both significant metropolises of the area – Philippopolis and Beroe/Augusta Traiana. Moreover, the mountain's Southern slopes looking towards the Upper Thracian Plain were more densely populated partly because of its geographical disposition and partly because of climatic reasons.

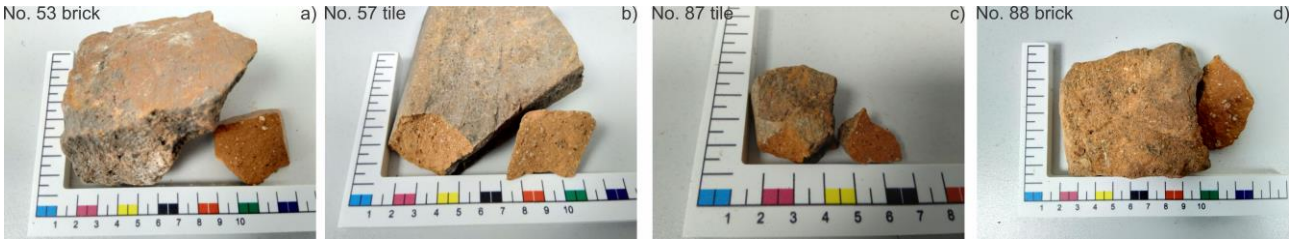

Figure 1. Roman ceramic.

Figure 2. Late Antique ceramic

Figure 3. Geographical location of the archaeological sites. Yellow lines are borders and southern is Greece

The sampling sites belong to two general types – open settlements and fortified ones (hillforts). Besides vicus, site No. 8 Pizos also had the status of Emporion and continued its function till the middle of 6th c. AD as phrourion (fortress), not located yet (Boyanov, 2014). Site No. 6 – the Roman vicus at Malko Tranovo was a huge agglomeration of many households and probably a significant center of agriculture, situated between the mansio of Karasura and Beroe/Augusta Traina (Wendel, 2001; Dumanov, 2004). In the late 4th c. AD two sites shared the same destiny - abandonment, as their population migrated toward the foothills or upland zones. The location of fortified settlements of sampling was at the highland (No. 10; 14-17) and uplands (No. 19) of Karaca Dağı. They reflect the transformation of settlement models before and after the period of political, social, and economic transitions from the middle 5th c. AD. In the fortified settlements, ceramics were rarely used in the fortifications', but mainly for the roofs and floor isolation of the churches and the households.

Table 1 shows the geographical location, type of archaeological sites, and the ceramic samples' description (macro and micro observations by microscope Levenhuk 3ST, 20-40x optical zoom). The geological settings of the area were described in detail elsewhere (Kostova et al., 2022).

Table 1. Short description of the archaeological sites and their respective ceramic samples.

Archaeological site		Ceramic samples		
No./location	Type	No.	Type	Macro and micro description
		Roman Age		
Site No. 8 Dimitrievo village	Open settlement (*Emporion Pizos*)	53	floor brick	Thickness: 4 cm. Surfaces: smooth upper and rough lower; lime mortar traces on rough and side surfaces Color: uniform orange-brown. Structure – porous fine-grained matrix with medium-grained inclusions. Inclusions composition: mainly quartz, a subordinate quantity of muscovite, feldspar (?). Inclusions size: from 1 mm up to 5-6 mm.
		57	roof tile	Thickness: 3 cm. Surfaces: smooth. Color: uniform beige with an orange tint. Structure – porous fine-grained matrix with medium-grained inclusions. Inclusions composition: mainly calcite, a subordinate quantity of quartz. Inclusions size: from 1 mm up to 5-6 mm.
Site No. 6 Malko Tranovo village, 1.10 km North from the village center	Open settlement (*vicus*)	87	roof tile	Thickness: 2 cm. Surfaces: smooth. Color: uniform orange-brown. Structure – porous fine-grained matrix with medium-grained inclusions. Inclusions composition: mainly quartz, a subordinate quantity of feldspar and muscovite. Inclusions size: up to 2 mm.
		88	floor brick	Thickness: 2 cm. Surfaces: smooth upper and rough lower. Color: uniform orange-brown. Structure – porous fine-grained matrix with medium-grained inclusions. Inclusions composition: mainly quartz; subordinate quantity of muscovite. Inclusions size: from 1 mm up to 10 mm.

		Late Antiquity		
Site No. 14 Gorno Novo Selo village, Sveti Nikola region	Fortified settlement - preserved stone fortress, church building, and traces of apse.	2	roof tile	Thickness: 3 cm. Surfaces: smooth upper and rough lower. Color: uniform orange-brown. Structure – porous fine-grained matrix with medium-grained inclusions. Inclusions composition: mainly quartz, a subordinate quantity of feldspar and muscovite. Inclusions size: from 1 mm up to 5-6 mm.
		3	floor brick	Thickness: 4 cm. Surfaces: smooth upper and rough lower; preserved lime mortar on rough and side surfaces. Color: uniform orange-brown. Structure – porous fine-grained matrix with medium-grained inclusions. Inclusions composition: mainly quartz, a subordinate quantity of feldspar and muscovite. Inclusions size: from 1 mm up to 5-6 mm.
Site No. 15 Gorno Novo Selo village, Kutchuk kale region	Fortified settlement (church *Extra Muros 1*) - preserved stone church and buildings walls	5	roof tile	Thickness: 2.5 – 3 cm. Surfaces: smooth. Color: uniform orange-brown. Structure – porous fine-grained matrix with medium-grained inclusions. Inclusions composition: mainly quartz, muscovite, feldspar (?). Inclusions size: from 1mm up to 4-5 mm.
		6	floor brick	Thickness: 4 cm. Surfaces: smooth upper and rough lower. Color: uniform orange-brown. Structure – porous fine-grained matrix with medium-grained inclusions. Inclusions composition: mainly quartz, a subordinate quantity of muscovite, feldspar (?). Inclusion size: from 1mm up to 5-6 mm.
Site No. 17 Gorno Novo Selo village	Fortified settlement - preserved stone fortress and building walls	8	roof tile	Thickness: 2 cm. Surfaces: smooth upper and rough lower. Color: uniform orange-brown. Structure – porous fine-grained matrix with medium-grained inclusions. Inclusions composition: mainly quartz, a subordinate quantity of muscovite. Inclusions size: from 1 mm to 3-4 mm.
		12	floor brick	Thickness: 4 cm. Surfaces: smooth upper and rough lower. Color: uniform orange-brown. Structure – porous fine-grained matrix with medium-grained inclusions. Inclusions composition: quartz, muscovite, feldspar, rock fragments (gneiss). Mineral inclusions predominate in quantity. Inclusions size: from 1 mm up to 10 mm.
Site No. 16 Gorno Novo Selo village, 2.1 km West from the village	Fortified settlement (church *Extra Muros 2*) - preserved stone church and buildings walls	20	floor brick	Thickness: 5 cm. Surfaces: smooth upper and rough lower; preserved lime mortar on rough and side surfaces. Color: uniform orange-brown. Structure – porous fine-grained matrix with medium-grained inclusions. Inclusions composition: quartz, muscovite, rock fragments. Mineral inclusions predominate in quantity. Inclusions size: mineral grains – 1 to 3 mm, rock fragments – up to 10 mm.
		21	roof tile	Thickness: 2.5 cm. Surfaces: smooth. Color: uniform orange-brown. Structure – porous fine-grained matrix with medium-grained inclusions. Inclusions composition: quartz, muscovite. Inclusions size: from 1 mm up to 10 mm.
Site No. 10 Izvorovo village, Golyamoto gradishte area	Fortified settlement - preserved stone fortress	71	floor brick	Thickness: 2.5 cm. Surfaces: smooth upper and rough lower. Color: uniform beige with an orange tint. Structure – porous fine-grained matrix with medium-grained inclusions. Inclusions composition: quartz, muscovite, feldspar, calcite. Inclusions size: from 1 mm to 5-6 mm.
		72	roof tile	Thickness: 3 cm. Surfaces: smooth upper and rough lower. Color: uniform orange-brown. Structure – porous fine-grained matrix with medium-grained inclusions. Inclusions composition: quartz and muscovite. Inclusions size: from 1 mm to 2-3 mm.
Site No. 19 Dolno Novo Selo village, 0.56 km from the village center	Fortified settlement - no preserved archaeological structures, stone blocks and ceramic not in situ.	140	floor brick	Thickness: 3.5 cm. Surfaces: smooth upper and rough lower; preserved lime mortar on rough and side surfaces. Color: uniform orange-brown. Structure – porous fine-grained matrix with medium-grained inclusions. Inclusions composition: quartz, muscovite, feldspar. Inclusions size: from 1 mm to 3-4 mm.
		141	roof tile	Thickness: 2.5 cm. Surfaces: smooth. Color: uniform orange-brown. Structure – porous fine-grained matrix with medium-grained inclusions. Inclusions composition: mainly quartz, a subordinate quantity of muscovite. Inclusions size: from 1 mm to 3-4 mm.

2.2. *Methods*

Sample preparation: all the studied samples were manually dry milled in porcelain and agate mortars and homogenized. The lime mortar, detected at No. 53 (Fig. 1a), No. 3, No. 20, and No. 140 (Fig. 2b, 2g, 2k), was not included in the milled samples.

X-ray fluorescence (XRF) analysis was performed by spectrometer WD-XRF Supermini 200 - Rigaku, Japan (50 kV and 4mA, 200 W X-ray tube with Pd-anode, 30 mm²) in a helium atmosphere. Two different X-ray detectors, a gas flow proportional counter for light elements and a scintillation counter for heavy elements are used. Depending on the wavelength range, two analysing crystals: LIF 200 (for Ti-U), PET (for Al-Ti) and RX25 (for F-Mg) were used. The software package ZSX used for data processing. The samples were prepared as tablets with CEREOX-BM-0002-1 powder.

The powder X-ray diffraction (PXRD) measurements were made by D2 Phaser BrukerAXS, CuKα radiation (λ = 0.15418 nm) (operating at 30 kV, 10 mA) from 3 to 70°2θ with a step of 0.05°, 1 s/step (ground sample weight – 1.0±0.1 mg and particle size below

0.075 mm). The PDF database was used for determining the phases and minerals in the samples (Powder Diffraction File, 2001).

Fourier transform infrared (FTIR) measurements were performed by FTIR Spectrometer Nicolet 6700, covering the range of 400 - 4000 cm^{-1} with 100 scans and 1.928 cm^{-1} resolution. The samples were prepared as pellets with KBr.

Thermal analysis: simultaneous TG/DTG-DSC analysis was carried out on a Setline STA 1100, SETARAM, France, in the temperature range room temperature (RT) – 1050°C; in the static air, with a heating rate of 10°C min^{-1}. The operational characteristics of the TG/DTG–DSC - system were: sample mass of 25.0±1.0 mg (mass resolution of 0.05 μg), temperature resolution of +/- 0.3°C, and alumina sample crucible with a volume of 100 μL.

3. RESULTS

3.1. XRF

Table 2 shows the results of the XRF analysis. The SiO_2 and Al_2O_3 are the highest concentrations in the studied samples except sample No. 57. The SiO_2 varies from 52.05 (No. 57) to 66.60% (No. 2), the Al_2O_3 - from 14.91 (No. 57) to 20.98% (No. 6). The alkali metals' concentrations also fluctuate - K_2O from 3.42 (No. 71) to 5.07% (No. 12), Na_2O - from 0.64 (No. 57) to 1.88% (No. 8). The greatest measured variations were for CaO - from 1.77 (No. 21) to 20.70% (No. 57). The lowest values of SiO_2 and Al_2O_3 correspond to the highest CaO concentration and were measured in samples No. 57 and No. 71. The MgO changes insignificantly – from 1.27 to 2.31%. The Fe_2O_3 is between 3.97 and 6.28%. The TiO_2, MnO, P_2O_5, and SO_3 are in low concentrations.

The SiO_2 and Al_2O_3 concentrations suggest a predominance of silicate and aluminosilicate phases. The alkali metals assume the existence of potassium and sodium aluminosilicates such as illite, muscovite, potassium feldspar, and plagioclase. The CaO concentration suggests the presence of carbonates and calcium aluminosilicates, such as calcite, feldspar, and smectite clays. The Fe may be due to iron phases and/or iron being isomorphically incorporated in aluminosilicates. The Ti and Mn probably substitute other metals isomorphically.

Table 2. XRF results.

Site/ No.	Sample	Mass/ %											SiO_2/ Al_2O_3 ratio
		SiO_2	Al_2O_3	Na_2O	K_2O	MgO	CaO	TiO_2	MnO	Fe_2O_3	P_2O_5	SO_3	
Roman ceramic													
8	No. 53 brick	64.56	19.61	1.78	4.65	1.31	2.18	0.66	0.10	4.80	0.19	0.03	3.29
	No. 57 tile	52.05	14.91	0.64	3.43	1.40	20.70	0.64	0.17	5.53	0.31	0.09	3.49
6	No. 87 tile	64.35	19.16	1.54	4.53	1.51	2.24	0.73	0.12	5.50	0.22	-	3.36
	No. 88 brick	65.52	18.58	1.66	4.30	1.39	2.52	0.72	0.09	4.91	0.21	-	3.53
Late Antique ceramic													
14	No. 2 tile	66.60	19.51	1.41	4.14	1.27	2.19	0.66	0.07	3.97	0.11	-	3.41
	No. 3 brick	66.39	18.86	1.38	3.99	2.00	2.22	0.73	0.08	4.12	0.10	0.02	3.52
15	No. 5 tile	61.11	21.46	1.04	4.97	1.89	1.89	0.80	0.11	6.45	0.17	-	2.85
	No. 6 brick	63.19	20.98	1.34	4.98	1.37	1.87	0.72	0.09	5.20	0.17	-	3.01
17	No. 8 tile	64.52	20.25	1.88	4.17	1.43	1.80	0.64	0.10	4.72	0.39	-	3.19
	No. 12 brick	61.07	20.48	1.10	5.07	2.23	2.46	0.90	0.10	6.29	0.19	-	2.98
16	No. 20 brick	63.89	18.90	1.69	5.04	1.58	2.01	0.78	0.08	5.71	0.19	0.02	3.38
	No. 21 tile	62.37	20.59	1.08	4.91	1.81	1.77	0.76	0.08	6.28	0.23	0.03	3.03
10	No. 71 brick	57.28	16.72	0.89	3.42	1.62	13.20	0.69	0.17	5.53	0.27	0.07	3.43
	No. 72 tile	64.78	20.25	0.90	4.35	1.42	1.57	0.86	0.11	5.37	0.24	0.03	3.20
19	No. 140 brick	63.23	20.77	0.93	4.52	2.31	1.39	0.64	0.10	5.86	0.16	-	3.04
	No. 141 tile	64.77	19.25	1.42	4.48	1.91	1.92	0.68	0.10	4.96	0.36	0.03	3.36

3.2. PXRD

The results of the PXRD analysis are shown in Fig. 4 and Table 3. The registered phases were separated into three groups – clay minerals, accessory minerals, and impurity minerals (Meyers and Speyer, 2003).

Table 3. PXRD results.

Phase	Archaeological site and sample No.															
	Roman age				Late Antiquity											
	Site No. 8		Site No. 6		Site No. 14		Site No. 15		Site No. 17		Site No. 16		Site No. 10		Site No. 19	
	No. 53	No. 57	No. 87	No. 88	No. 2	No. 3	No. 5	No. 6	No. 8	No. 12	No. 20	No. 21	No. 71	No. 72	No. 140	No. 141
Illite/muscovite	+	+	+	+	+	-	+	+	+	+	+	+	+	+	+	+
Montorillonite	+	+	-	-	+	-	+	+	+	+	-	+	+	+	+	+
Glauconite	-	-	-	-	+	-	-	-	-	-	-	+	-	-	-	-
Chlorite	-	-	-	-	-	-	-	-	-	-	-	-	-	-	-	+
Hematite	+	+	+	+	+	+	+	+	+	+	+	+	+	+	+	+
Magnetite	-	+	-	-	+	-	+	+	+	+	+	+	+	-	-	-
Quartz	+	+	+	+	+	+	+	+	+	+	+	+	+	+	+	+
Plagioclase	+	+	+	+	+	+	+	+	+	+	+	+	+	+	+	+
K-feldspar	+	+	+	+	+	+	+	+	+	-	+	+	-	+	-	-
Amphibole	-	-	-	-	-	-	-	-	-	-	-	-	+	-	-	+
Calcite	-	+	-	-	-	-	-	-	-	-	-	-	+	-	-	-

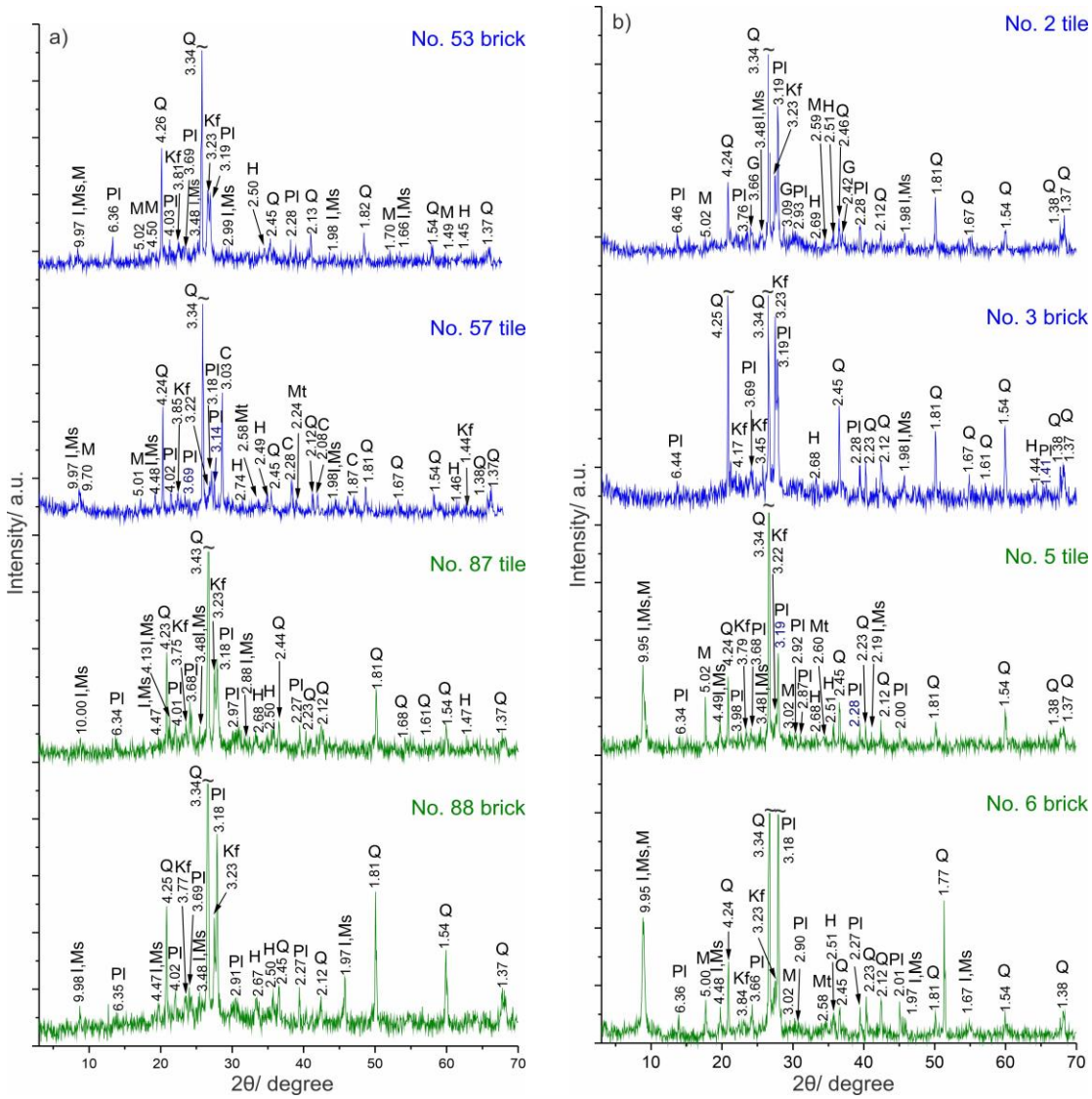

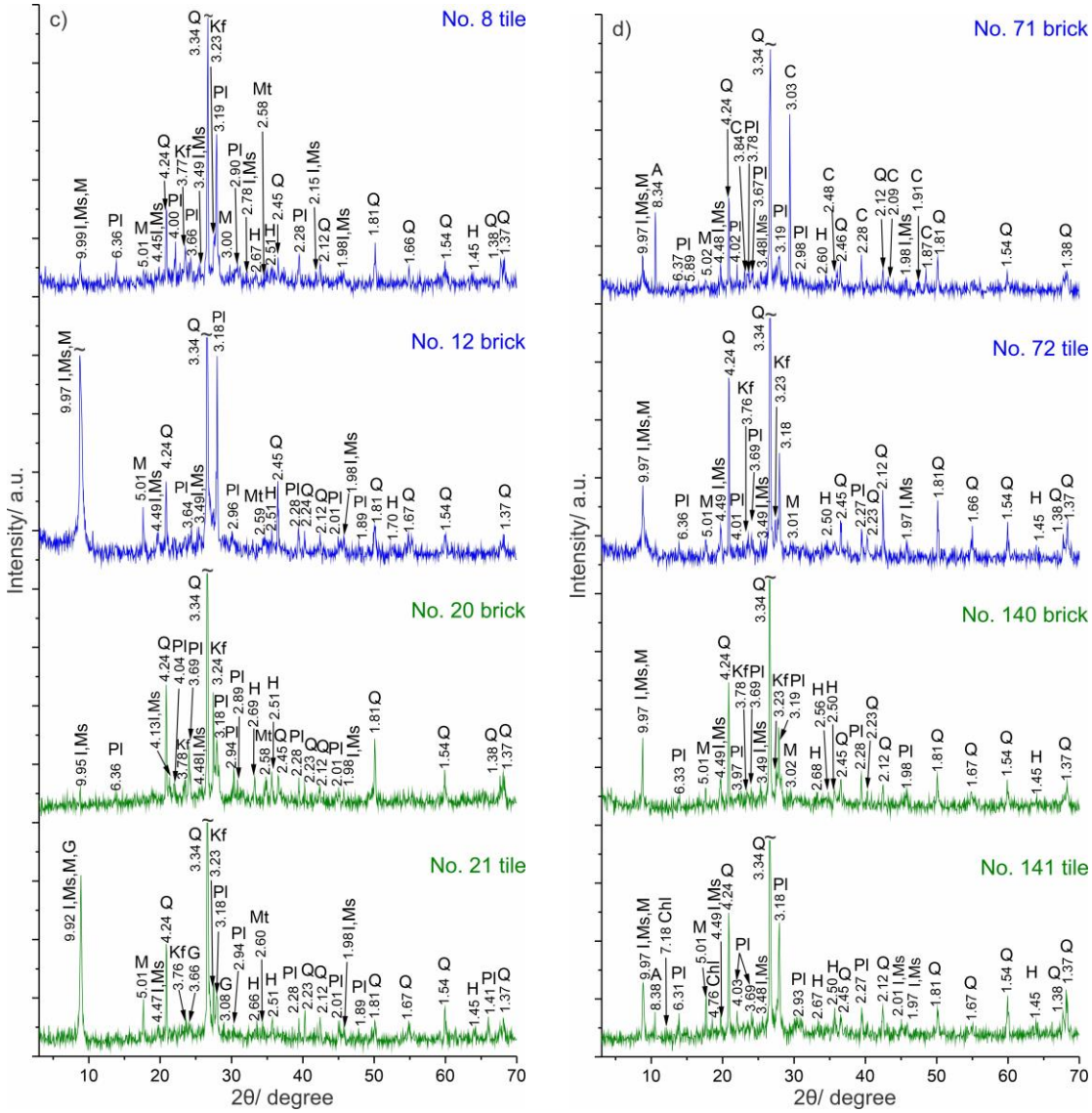

Figure 4. PXRD patterns of samples: a) No. 53 and No. 57 (site No. 8), No. 87 and No. 88 (site No. 6); b) No. 2 and No 3 (site No. 14), No. 5 and No. 6 (site No. 15); c) No. 8 and No. 12 (site No. 17), No. 20 and No. 21 (site No. 16); d) No. 71 and No. 72 (site No. 10), No. 140 and No. 141 (site No. 19). Q – quartz, I – illite, Ms – muscovite, Kf – potassium feldspar, Pl – plagioclase feldspar, H – hematite, Mt – magnetite, M – montmorillonite, G – glauconite, C – calcite, A – amphibole, Chl – chlorites.

The diagnosed clay minerals are illite $(K_{0.65}A_{l2}[Al_{0.65}Si_{3.35}O_{10}](OH)_2$ (PDF #25-0001), glauconite, $(K,Na)(Fe^{3+},Al,Mg)_2(Si,Al)_4O_{10}(OH)_2$ (PDF #45-1337), and montmorillonite $(Na,Ca)_{0.33}(Al,Mg)_2(Si_4O_{10})(OH)_2nH_2O$ (PDF #302-0239). Accessory minerals are muscovite $KAl_2(AlSi_2O_{10})(OH)_2)$ (PDF #34-0175) and chlorite $(Mg,Al,Fe)_6(Si,Al)_4O_{10}(OH)_8$ (PDF #78-2063). The impurities are quartz SiO_2 (PDF #06-175), potassium feldspar - microcline, $KAlSi_3O_8$ (PDF #84-0710), plagioclase – albite $NaAlSi_3O_8$ (PDF #89-6426), hematite Fe_2O_3 (PDF #72-0469), magnetite $(Fe^{2+}Fe^{3+}{}_2O_4)$ (PDF#19-0629), amphibole $NaCa_2(Mg,Fe,Al)_5(Si,Al)_8O_{22}(OH)_2$ (PDF #73-1135), and calcite $CaCO_3$ (PDF #47-1743). Quartz, plagioclase, and hematite were proven in all samples. Illite/muscovite was evidenced in all samples except No. 3. Illite and muscovite, being isostructural (2:1 layer silicates designed of two tetrahedral sheets with one octahedral sheet situated between the tetrahedral ones), have coinciding PXRD peaks making it difficult to distinguish them by this method (Kotryová et al., 2016; Chamley, 1989). On the other hand, the 9.97Å peak of illite/muscovite also coincides with that of heated montmorillonite (after heating, the water molecules from interlayer space disappear and a reduction of d_{001} is realized from 14.5Å up to 9.80Å) (Khalifa et al., 2019; Laufek et al., 2021). Montmorillonite was proven in most of the samples, except No. 87, 88,

3, and 20. Potassium feldspar was not detected only in No. 12, 71, 140, and 141. Magnetite was not recognized in No. 53, 87, 88, 3, 72, 140, and 141. Chlorite, glauconite, and amphibole were found in single samples: chlorite in No. 141, glauconite in No. 2 and No. 20, and amphibole – in No. 71 and No. 141. The carbonate phase, calcite, was proven only in samples No. 57 and No. 71.

The PXRD patterns of all samples have no increased background noise (Fig. 4), which suggests the absence of amorphous (vitrified) phases (Cultrone et al., 2001; Elert et al., 2003).

3.3. *FTIR*

Fig. 5 shows the results of the FTIR analysis. The obtained results confirm the PXRD results, complementing them. By FTIR, the illite, muscovite, montmorillonite, glauconite, magnetite, potassium feldspar, and calcite were evidenced in all the examined samples.

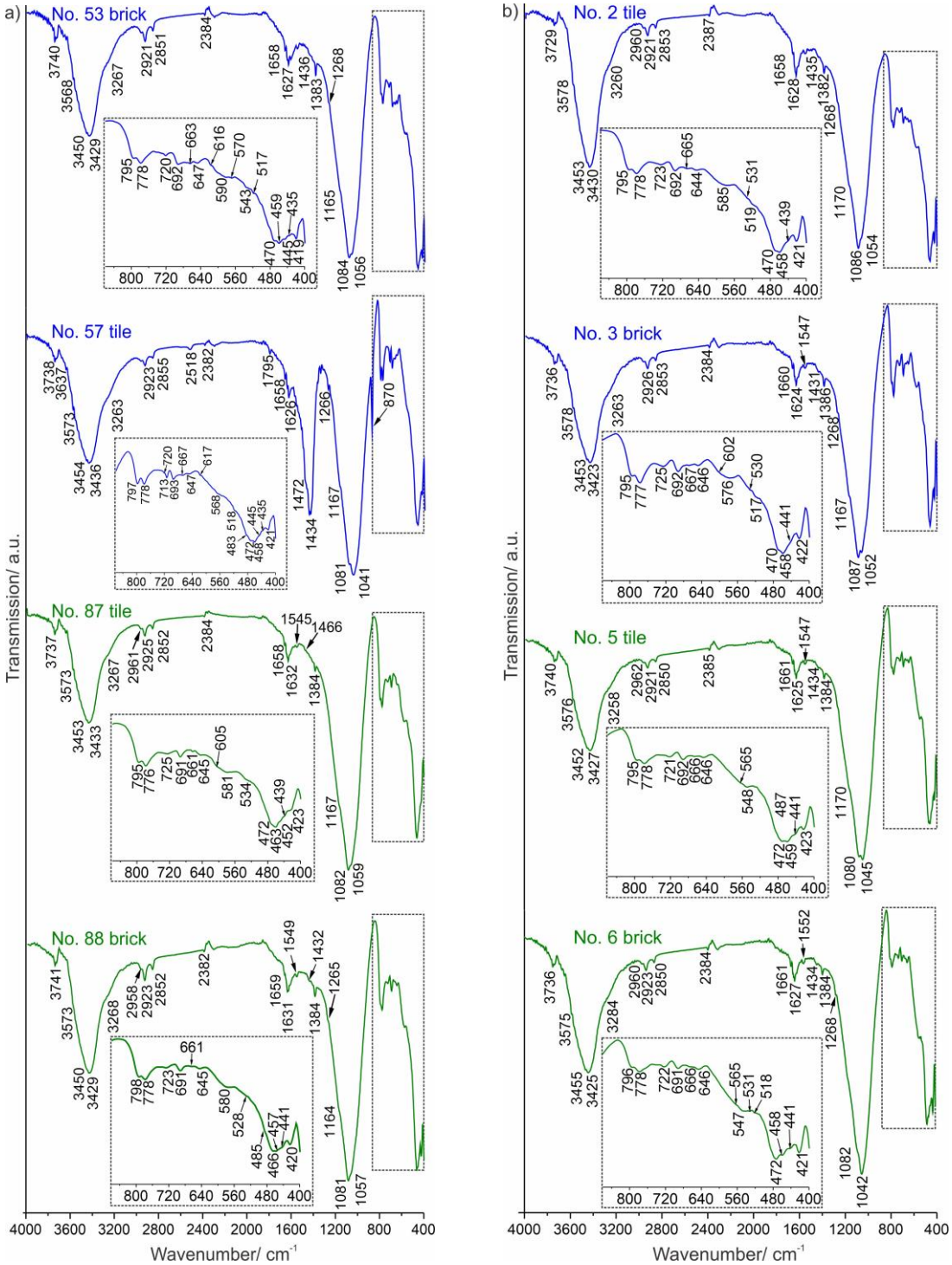

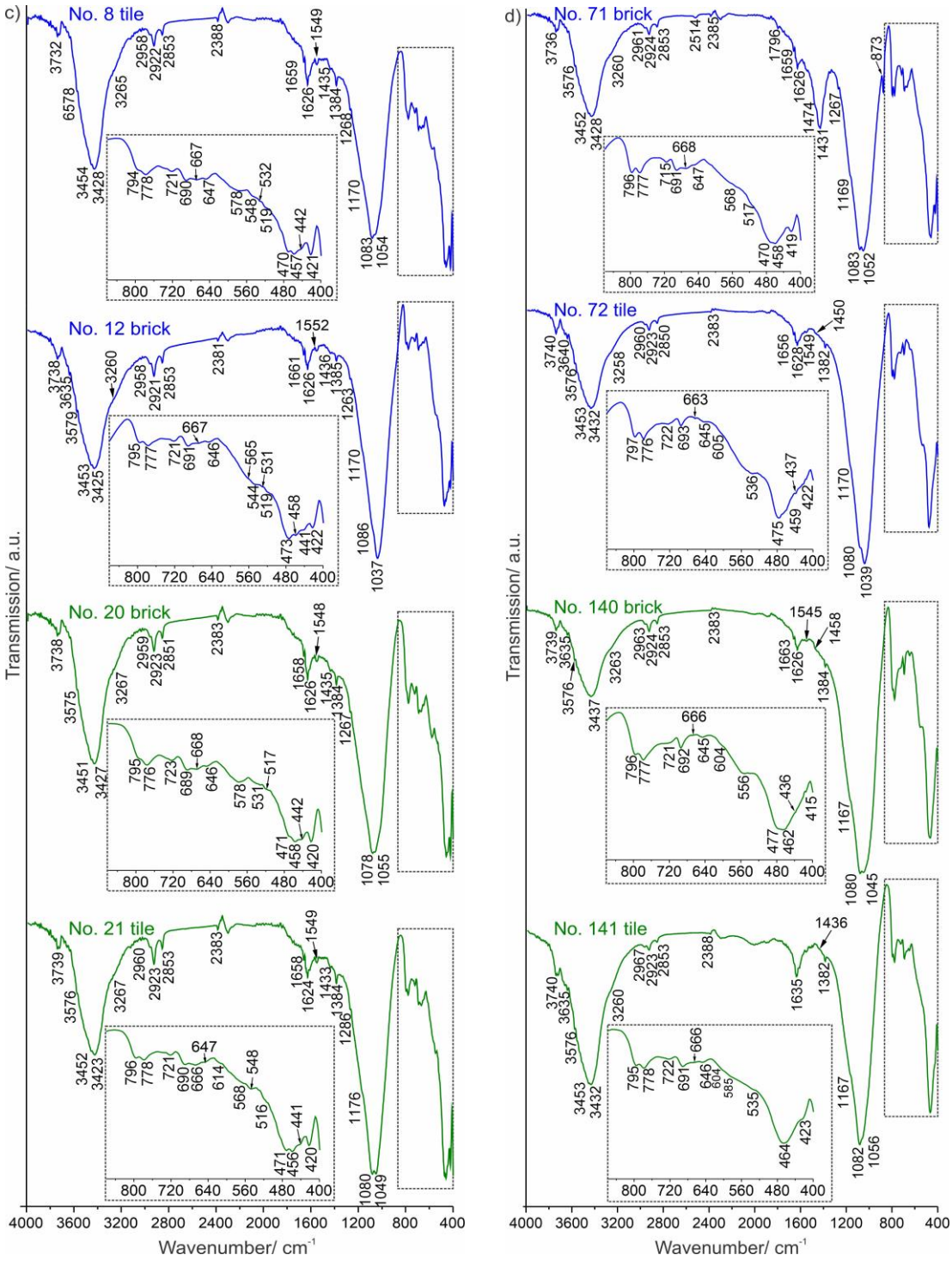

Figure 5. FTIR spectra of samples: a) No. 53 and No. 57 (site No. 8), No. 87 and No. 88 (site No. 6); b) No. 2 and No 3 (site No. 14), No. 5 and No. 6 (site No. 15); c) No. 8 and No. 12 (site No. 17), No. 20 and No. 21 (site No. 16); d) No. 71 and No. 72 (site No. 10), No. 140 and No. 141 (site No. 19). Insertions: 860 – 400 cm^{-1} spectral region.

Illite, muscovite, montmorillonite, and glauconite were recognized with two types of bands - the first is characteristic only of a given mineral, and the second refers to more than one mineral. The band at 3635-3640 cm^{-1} was assigned to Al-OH stretching band of illite, montmorillonite, and glauconite (Yan et al., 2021; Chukanov, 2014); at 3568-3576 cm^{-1} – as OH stretching band of glauconite (Chukanov, 2014); at 3450–3453 cm^{-1} – as H-O-H stretching vibration of adsorbed water molecules in illite (Chukanov, 2014, Jozanikohan and Abarghooei, 2022); at 3429-3437 cm^{-1} – as H-O-H stretching vibration of adsorbed water molecules in montmorillonite (Chukanov, 2014, Jozanikohan and Abarghooei, 2022); at 3258–3268 cm^{-1} – as metal-O-H stretching vibration of montmorillonite (Caccamo et al., 2020); at 1658–1663 cm^{-1} – as

H-O-H bending vibration of adsorbed water molecules of illite (Palanivel and Rajesh Kumar, 2009; Chukanov, 2014); at 1626–1635 cm^{-1} – as O-H bending vibration of adsorbed water molecules of illite, muscovite and glauconite (Chukanov, 2014, Singha and Singh, 2016); at 1039-1056 cm^{-1} – as Si-O-Si asymmetric stretching vibration band of illite and montmorillonite (Yan et al., 2021; Chukanov, 2014); at 568-585 cm^{-1} – as Al-O-Al asymmetric bending vibration of illite and montmorillonite (Yan et al., 2021; Chukanov, 2014); at 517-519 cm^{-1} – as Al-O-Al symmetric bending vibration of muscovite (Chukanov, 2014); at 470–473 cm^{-1} – as Si-O-Si bending and the metal-O stretching vibrations in muscovite, illite, montmorillonite (Chukanov, 2014); and band at 435–441 cm^{-1} – as Si-O bending vibration of glauconite and illite (Chukanov, 2014).

The quartz was recognized with bands at 1165-1170 cm^{-1} and 1080-11087 cm^{-1} (v3 Si-O in SiO_2), at 795-797 cm^{-1} and 776-778 cm^{-1} (v2 Si-O in SiO_2), and at 689-693 cm^{-1} (v1 Si-O in SiO_2) (Chukanov, 2014). Alkali feldspar, albite, was detected by O-Si(Al)-O bending vibrations at 720–725 cm^{-1} and 602-614 cm^{-1}, O-Si-O deformation and K-O stretching vibration at 543-556 cm^{-1}, and Si-O-Si deformation vibration at 483-487 cm^{-1} (Chukanov, 2014; Theodosoglou et al, 2010). Potassium feldspar, microcline, was registered by O-Si-O bending and K-O stretching vibrations at 531-536 cm^{-1}, 463-466 cm^{-1}, and 445 cm^{-1}, and Si-O-Si deformation vibration at 419-423 cm^{-1} (Chukanov, 2014; Theodosoglou et al, 2010). Hematite was registered by Fe^{3+}-O vibrations at 645–647 cm^{-1} and 452-464 cm^{-1} (Chukanov, 2014; Jozanikohan and Abarghooei, 2022), where magnetite – by Fe^{2+}-O vibration at 663-668 cm^{-1} (Ravisankar et al., 2010; Chukanov, 2014). Calcite was recognized by bands at 2514-2518 cm^{-1} (v1+ v3) C-O in CO_3 (Chukanov, 2014), 1795–1795 cm^{-1} (v1 + v4) C-O in CO_3 (Chukanov, 2014; Stanienda, 2016), and 1466-1474 cm^{-1} and 1431-1458 cm^{-1} v3 C-O in CO_3, 870 - 872 cm^{-1} v2 C-O in CO_3, and 713-715 cm^{-1} v4 C-O in CO_3 (Chukanov, 2014).

Organic phases were evidenced in all samples. Bands at 2960-2967 cm^{-1} and - 2921–2925 cm^{-1} were recognized as C-H asymmetrical stretching vibrations of CH_2 and 2850-2853 cm^{-1} – as C-H symmetrical stretching vibrations in CH_2 (Silva et al., 2005; Rao et al., 2017). The bands at 1545-1549 cm^{-1} – as skeletal vibrations of the aromatic ring, bands at 1382–1385 cm^{-1} – as C-H bending vibrations of the methyl and methylene groups, and those at 1263-1268 cm^{-1} as v3 stretching vibration of C-O in aromatic rings (Rao et al., 2017).

The surface hydroxyl group was detected at 3733 – 3740 cm^{-1} - O-H vibration (Jozanikohan and Abarghooei, 2022; Chukanov and Chervonnyi, 2016). The band at 2382–2388 cm^{-1} was assigned to CO_2 from the air (Chukanov and Chervonnyi, 2016).

3.4. *Thermal analysis*

Figure 6 and Table 4 show the results of the thermal analysis. The measured total mass loss (ML_{tot}) was changed from 3.04% for sample No. 88 to 11.98% for No. 57.

Table 4 Thermal analysis results.

Sample	RT - 220°C dexydration				220°C - 420°C organic decomposition		420°C - 720°C dehydroxylation		720°C - 840°C decarbonation		840°C -1050°C structure destruction	
	T_{infl}/ °C	ML/ %	T_{infl}/ °C	ML/ %	T_{infl}/ °C	ML/ %	T_{infl}/ °C	ML/ %	T_{infl}/ °C	ML/ %	T_{infl}/ °C	ML/ %
Roman age												
No. 53	31.7	0.37	164.3	0.39	240.5	0.55	522.8	0.24	783.5	0.14	849.0	0.40
	73.9	0.33			312.1	0.30	672.0	0.34			986.6	0.23
					374.0	0.31					1034.0	0.36
No. 57	31.7	0.17	135.8	1.33	251.8	0.33	454.1	0.39	775.0	3.62	903.0	0.12
	77.5	0.43	208.4	0.45	295.7	0.24	524.5	0.41			961.2	0.13
					365.3	0.56	586.5	0.53			1017.4	0.24
							670.9	1.76				
							700.6	1.00				
No. 87	40.0	1.20	130.4	0.40	251.6	0.56	447.3	0.47	783.3	0.24	876.5	0.46
	104.8	0.26	202.3	0.59	301.4	0.58	563.4	0.40			985.9	0.69
					365.48	0.58	642.7	0.49			1028.3	0.43
							720.2	0.46				
No. 88	39.9	0.68	169.4	0.13	323.5	0.23	462.4	0.15	783.3	0.20	877.3	0.20
					387.6	0.18	523.9	0.13			956.1	0.22
							673.3	0.42			1020.1	0.40
Late Antiquity												
No. 2	57.8	0.36	122.1	0.16	274.6	0.53	492.8	0.64	807.8	0.26	864.9	0.27
			205.8	0.55	315.9	0.21	549.6	0.61			919.9	0.09
					355.2	0.24	687.3	0.10			1003.2	0.20
					392.0	0.27					1037.3	0.35
No. 3	50.0	0.46	106.9	0.21	259.4	0.46	475.5	0.40	797.1	0.30	856.6	0.32

	73.7	0.37	149.6	0.38	313.0	0.43	551.8	0.42			1013.6	0.41
			201.8	0.57	376.6	0.39	658.1	0.30			1036.6	0.21
							691.1	0.31				
No. 5	52.1	0.60	110.2	0.15	272.5	0.57	438.9	0.34	801.5	0.23	863.0	0.27
			144.9	0.20	357.1	0.47	521.3	0.45			992.0	0.47
			194.4	0.64			683.5	0.67			1047.5	0.30
No. 6	50.2	1.00	108.6	0.37	246.4	0.42	452.6	0.53	797.5	0.15	867.0	0.35
			140.4	0.52	304.5	0.58	522.5	0.29			956.5	0.13
			189.9	0.38			589.0	0.22			1033.3	0.49
							673.7	0.47				
No. 8	78.7	0.9	153.4	0.50	295.5	1.71	441.6	0.51	798.3	0.30	861.1	0.31
			188.0	0.46			544.2	0.46			986.1	0.27
			215.5	0.25			691.8	0.60			1022.2	0.30
No. 12	69.0	0.47	126.8	0.35	312.8	0.36	459.2	0.54	799.0	0.24	894.3	0.50
	101.2	0.44	150.3	0.28	384.9	0.45	526.7	0.42			986.1	0.37
			177.8	0.42			573.2	0.29			1042.2	0.30
							686.3	0.63				
No. 20	60.4	0.60	112.1	0.13	264.9	0.96	448.2	0.33	807.9	0.27	859.7	0.45
			138.5	0.31	372.8	0.40	521.5	0.18			1006.5	0.33
			207.9	0.46			665.3	0.73			1039.9	0.06
No. 21	48.6	0.20	145.8	0.31	295.0	0.30	457.2	0.24	798.3	0.15	861.6	0.30
	70.9	0.18	210.6	0.53	375.4	0.20	566.1	0.20			935.1	0.10
							648.4	0.16			1020.5	0.46
							685.1	0.28				
No. 71	64.7	0.54	119.0	0.36	237.6	0.11	462.9	0.12	768.4	3.44	883.8	*
			193.5	0.28	285.3	0.16	521.5	0.11			979.3	*
					321.8	0.10	567.3	0.17			1012.2	*
					364.5	0.08	673.5	0.65				
No. 72	62.8	1.32	142.0	0.50	273.2	0.13	458.4	0.99	801.1	0.20	882.2	0.35
			188.0	0.60	374.0	0.49	568.4	0.31			997.5	0.29
							684.4	0.58			1024.5	0.24
No. 140	59.2	1.17	189.0	0.65	252.5	0.67	462.0	0.26	802.8	0.23	874.2	0.37
					312.1	0.40	493.2	0.17			989.9	0.64
					378.9	0.45	521.4	0.13			1034.0	0.16
							680.2	0.67				
No. 141	51.7	0.30	125.7	0.11	295.9	0.13	476.0	0.61	803.5	0.27	867.3	0.36
	71.38	0.44	160.5	0.51	379.4	0.58	574.1	0.35			991.3	0.32
							668.7	0.62			1012.9	0.14
											1034.0	0.19

T_{infl} – temperature of the point of inflection/ °C
ML – mass loss/ %
* The effects are of small ML and cannot be measured correctly.

Five temperature ranges of thermal decomposition were recognized: RT-220°C (dehydration), 220-420°C (organic decomposition), 420-720°C (dehydroxylation), 720-840°C (decarbonation), and 840-1050°C (structure destruction).

RT - 220°C (dehydration): ML was measured in the dehydration temperature range from 0.81% (for sample No. 88) to 2.45% (for No. 87) (Table 4). Up to 100°C, the physically adsorbed water molecules evaporate (Moropoulou et al., 1995; Ion et al., 2010) with ML from 0.36% for No. 2 to 1.59% for No. 5 (Table 4). In the 100°C and 220°C temperature range, the phyllosilicates muscovite, illite, montmorillonite, and glauconite dehydrate. During this process, realization of the interlayered water occurs (Meyers and Speyer, 2003; Földvári, 2011).

220°C - 420°C (organic decomposition): Between 220 and 420°C, organic matter decomposition occurs at several stages (Palanivel et al., 2009; Imman et al., 2021). The decomposition was associated with an exothermic effect with a DSC curve peak at a temperature from 332.9°C (No. 71) to 342.7°C (No. 21) (Fig. 6), with a few DTG curve peaks and a total ML from 0.37% (No. 71) to 1.71% (No. 8) (Table 4).

420°C - 720°C (dehydroxylation): During this temperature range, the following three thermal processes occur:

- magnetite oxidation, recognized by exothermic DSC curve peak between 504.7°C (No. 5) and 527.1°C (No. 140) and DTG curve peak with T_{infl} from 443.7°C (No. 2) to 510.3°C (No. 12) (Fig. 6) (Földvári, 2011). Such a process was not detected only in sample No. 141.

- α-β quartz transition without ML (Moropoulou et al., 1995). The process was registered in all the studied samples with a DSC curve peak situated between 571.1°C (No. 20, No.141) and 573.1°C (No. 3, No. 71) (Fig. 6).

- dehydroxylation of the phyllosilicates, which was recorded in all samples. The dehydroxylation occurred with ML of 0.40% in sample No. 71 to 4.09% at

No. 57 (Table 4). Illite, montmorillonite, glauconite, and muscovite, being dioctahedral 2:1 layer silicates, can re-hydroxylate with time at a lower temperature (Kotryová et al., 2016; Hamilton and Hall, 2012; Muller et al., 2000). Such a feature allows the thermal process to be registered in the archaeological ceramic as follows: montmorillonite dehydroxylation occurs between 440°C - 490°C (Meyers and Speyer, 2003; Laufek et al., 2021); in the 520°C - 590°C interval, illite and glauconite dehydroxylate (Földvári, 2011; Hatakeyama and Liu, 1998; Marsh et al, 2018), at 670°C - 690°C - a muscovite dehydroxylation occurs (Földvári, 2011; Velosa et al., 2007; Pei et al., 2018) (Table 4).

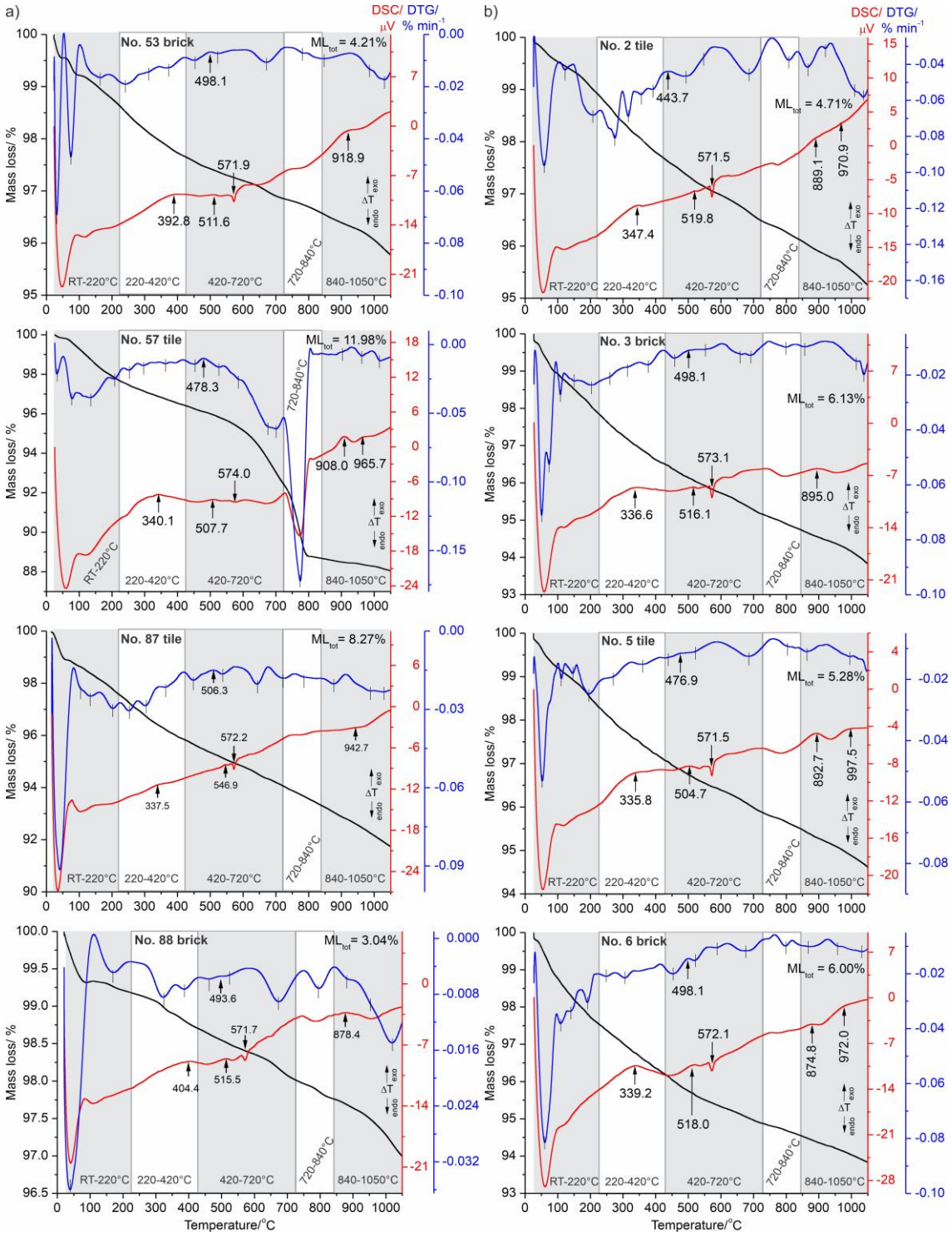

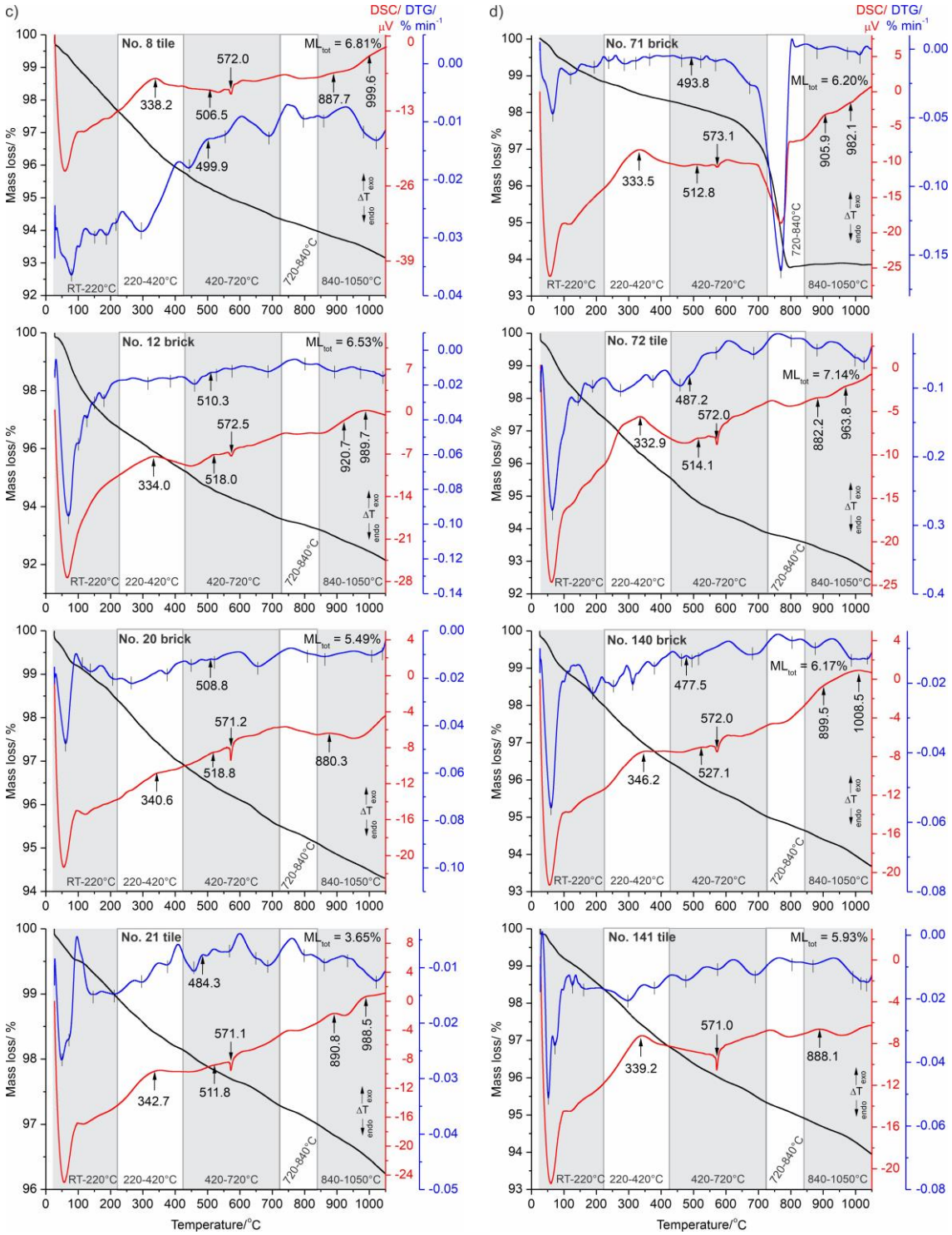

Figure 6. TG, DTG, and DSC curves of samples: a) No. 53 and No. 57 (site No. 8), No. 87 and No. 88 (site No. 6); b) No. 2 and No 3 (site No. 14), No. 5 and No. 6 (site No. 15); c) No. 8 and No. 12 (site No. 17), No. 20 and No. 21 (site No. 16); d) No. 71 and No. 72 (site No. 10), No. 140 and No. 141 (site No. 19).

720°C - 840°C (decarbonation): In this temperature range, calcite decarbonation was recognized (Böke et al., 2006). The decarbonation was detected for all samples (Fig. 6, Table 4), which confirms the results of FTIR (Fig. 5). The calcite decarbonation temperature changes from 768.4°C (for sample No. 71) to 807.9°C (sample No. 20), and the ML – from 0.14% (No. 53) to 3.62% (No. 57).

From the measured ML_{CO2}/ % during calcite decomposition, the amount of CaO and $CaCO_3$ in the samples was calculated (Table 5). The obtained results show that the quantity of calcite is low - from 0.30% to 0.68% for most samples, which explains the registration of calcite only by FTIR (Fig. 5). Exceptions are samples No. 57 and No. 71 with calcite of 8.20% and 7.79%, respectively. For these two samples calcite

was also detected by PXRD (Table 3, Fig.-4). The calculations made show that only a small part of the total CaO was incorporated into calcite.

840°C - 1050°C (structure destruction): The dehydroxylated phyllosilicates form stable phases until reaching the temperature of structure destruction (Lee et al., 2008; Pérez-Monserrat et al., 2021). In the studied samples, the illite structure decomposes at T_{infl} between 849.0°C and 903.0°C. After the destruction, an exothermic effect appears (DSC curve peak between 874.8°C and 942.7°C), associated with crystallization of high-temperature spinel-type phases (Meyers and Speyer, 2003; El Ouahabi et al., 2015) (Table 4, Fig. 6).

The structure destruction of muscovite, glauconite, and montmorillonite occurs with endothermic effects at T_{infl} from 919.9°C to 1012.9°C and T_{infl} between 1012.2°C and 1039.9°C (Hatakeyama and Liu, 1998) (Table 4, Fig. 6). The registered dehydroxylation takes place with a total ML of 0.49% for No. 57 to 1.17% for No. 12 and No. 140 (Table 4). An exothermic effect with a peak at 965.7°C - 1008°C was registered on the DSC curve (Fig. 6), which probably was related to the crystallization of mullite (El Ouahabi et al., 2015) and cristobalite (above 1000°C) (Lee et al., 2008).

Table 5. Measured CaO/ % and ML_{CO2}/ % and calculated CaO/ % and $CaCO_3$/ % by ML_{CO2}/ %.

Sample	XRF	TG/DTG	Calculated from ML	
	CaO/ % total	ML_{CO2}/ % from $CaCO_3$ decarbonation	CaO/ % in $CaCO_3$	$CaCO_3$/ %
		Roman ceramic		
No. 53 brick	2.18	0.14	0.18	0.32
No. 57 tile	20.70	3.62	4.61	8.20
No. 87 tile	2.24	0.24	0.31	0.54
No. 88 brick	2.52	0.20	0.25	0.45
		Late Antique ceramic		
No. 2 tile	2.19	0.26	0.33	0.59
No. 3 brick	2.22	0.30	0.38	0.68
No. 5 tile	1.89	0.23	0.29	0.52
No. 6 brick	1.87	0.15	0.19	0.34
No. 8 tile	1.80	0.30	0.38	0.68
No. 12 brick	2.46	0.24	0.31	0.54
No. 20 brick	2.01	0.27	0.34	0.61
No. 21 tile	1.77	0.15	0.19	0.34
No. 71 brick	13.20	3.44	4.38	7.79
No. 72 tile	1.57	0.20	0.25	0.45
No. 140 brick	1.39	0.23	0.29	0.52
No. 141 tile	1.92	0.27	0.34	0.61

4. DISCUSSION

4.1. Raw clay

The phase analysis proves montmorillonite, illite, and glauconite in the investigated samples. All these clay minerals are 2:1 type layered silicates that can survive firing to temperatures around 840°C – 900°C, forming stable dehydroxylated structures that can be re-dehydroxylated over time (Khalifa et al., 2019; Lee et al., 2008; Pérez-Monserrat et al., 2021). Clays are poly-mineral sediments (Chamley, 1989), and it is possible they also consist of clay minerals of structural type 1:1, namely kaolinite. Kaolinite dehydroxylates with structure breakdown and transformation into metakaolin at 450°C - 550°C (Meyers and Speyer, 2003; El Ouahabi et al., 2015; Hatakeyama and Liu, 1998). The new-formed metakaolin is structurally similar to kaolinite but unable to register from PXRD. After heating to 980°C, metakaolin transforms into spinel (Meyers and Speyer, 2003). All studied samples show a DSC peak at the mentioned temperature (Fig. 6). Such a peak also corresponds to the crystallization of spinel-type phases after the breakdown of the 2:1 type layered clay minerals (Hatakeyama and Liu, 1998). The establishment of the presence/absence of kaolinite in the raw clay was obtained by the XRF analysis. In clays containing 1:1 type layered silicates (kaolinite), the SiO_2/Al_2O_3 ratio is close to 1 while for 2:1 type clays (containing illite, montmorillonite, etc.), that ratio is greater than 1 (Khalifa et al., 2019; Laufek et al., 2021; Gonidanga et al., 2019; Carretero et al., 2002). The SiO_2/Al_2O_3 ratio changes from 2.85% (sample No. 5) to 3.53% (No. 88), indicating that the source clay was composed of 2:1 type clay minerals (Table 2).

In addition to the structural type of layered minerals, clays were also classified by their CaO content, determined by chemical analysis, assuming that the measured CaO content corresponds to carbonate minerals - calcite, dolomite, etc. (El Ouahabi et al., 2015). Regarding CaO, the clays' classification was: (i) calcareous with CaO above 5% and (ii) non-calcare-

ous - with CaO below 5% (Badica et al., 2022). The ceramic industry uses chemical analysis (XRF) of raw clay to predict the formation of new crystalline phases during firing (El Ouahabi et al., 2015), and studying archaeological ceramic composition can define the raw clay type. The XRF results (Table 2) show the studied ceramic was made of two clay types: calcareous (No. 57 and No. 71) and non-calcareous – all other samples. Nevertheless, the thermal analysis proves a small quantity of CaO incorporated in carbonates - i. e. calcite, even in the samples with high CaO (20.70% for No. 57 and 13.20% for No. 71), where CaO incorporated into calcite is below 5% (4.61% for No. 57 and 4.38 % for No. 71) (Table 5). These results show that: (i) the starting clay cannot be classified as calcareous or non-calcareous only by chemical analysis, and (ii) all the investigated samples were made of non-calcareous raw clay, regardless that in some of them the amount of CaO measured by XRF exceeded 5%.

XRF, PXRD, FTIR, and thermal analysis results lead to the determination of the mineral composition of raw clay with great accuracy. PXRD evidenced minerals with contents above 5% in the samples, FTIR and thermal analysis confirmed the presence of phases in lower concentrations, and XRF - successfully established whether kaolinite was present in the raw clay.

4.2. *Ceramic firing conditions*

The ceramic mineral composition is useful for the determination of the ceramic firing temperature (El Ouahabi et al., 2015). The impurity minerals quartz and feldspars are resistant up to 1000°C – 1100/1200°C (Papadopoulou et al., 2006; Aras and Kiliç, 2017). Both minerals are found in the studied ceramic samples, which define firing below this temperature. The phase analysis shows the absence of newly formed high-temperature phases in the ceramics, such as spinels, etc., whose formation begins at a temperature of about 950°C (El Ouahabi et al., 2015). This suggests that the firing temperature did not exceed this value. Thermal analysis results show the formation of new high-temperature phases at a temperature between 880°C and 920°C (Fig. 6), which indicates that the kiln temperature did not exceed such temperatures. After heating to 860°C, the montmorillonite PXRD reflections disappear completely, and those of illite/muscovite decrease in intensity (Drebushchak et al., 2005; Trindade et al., 2009). Montmorillonite was evidenced by PXRD in most samples, except No. 3, 20, 87, and 88, and illite was proven in all samples (Table 3). Montmorillonite was detected by FTIR in the latter samples which suggests a montmorillonite concentration below the PXRD limits of detection (PXRD detects phases in concentration over 5% (Moropoulou et al., 1995). Such results show firing below 860°C. Calcite was found in the samples and its decomposition temperature (between 768.4°C and 807.9°C) was recorded by thermal analysis (Table 4), which suggests that the firing temperature did not exceed the indicated temperatures.

The phyllosilicate's rehydroxylation ability over time excludes the possibility to use their dehydroxylation temperature for determining the ceramic firing temperature. The incorporated new hydroxyl groups create weaker chemical bounds in comparison to the original ones, which can only lower the dehydroxylation temperature when reheating the ceramic (Kotryová et al., 2016; Muller et al., 2000). To specify the firing temperature range, the FTIR-bands of illite and montmorillonite were used, namely the Si–O–Si stretching vibration band in the 1000 – 1100 cm^{-1} spectral range and Si–O–Al bending vibration band in the range of 510 - 580 cm^{-1} (Yan et al., 2021). Heating to 500°C leads to a band at 520 cm^{-1} in the FTIR spectrum. Upon heating above 500°C, the band at 520 cm^{-1} disappears. Heating above 700°C leads to the appearance of a new band at 570 cm^{-1} (Yan et al., 2021). In the 1000 – 1100 cm^{-1} spectral region, after montmorillonite and illite heating to 400°C, a band was registered at about 1030 cm^{-1}. After applied heating above 500°C, that band shifts to higher wavenumbers (Yan et al., 2021). The band at 520 cm^{-1} does not appear in the FTIR spectra of the studied samples (Fig. 5), which suggests a firing temperature above 500°C. That assumption was also confirmed by the position of the band from the 1000 – 1100 cm^{-1} spectral region, which shifted to a higher wavenumber (Fig. 5). Samples No. 72 and No. 140 have no band of illite and montmorillonite in the 510 - 580 cm^{-1} spectral region, which defines the firing temperature of these samples as in the range of 500°C - 700°C. The other samples registered a band at 568-585 cm^{-1}, indicating a firing temperature above 700°C but below calcite decarbonation temperature (Table 4).

It is shown that in order to determine the ceramic firing temperature range, it is necessary to use not only the phase composition (mineral-thermometers) but also the structural features of the minerals determined by FTIR and thermal analyses. For the studied samples, the approach determines the lower firing temperature limit by PXRD and FTIR and the upper limit by thermal analyses.

The determined firing temperatures show the lack of amorphous phases in the ceramic indicate that partial melting begins at about 900°C (Emami et al., 2016). That also confirms the observations of the PXRD patterns for the absence of amorphous (vitrified) phases in the investigated ceramics (Fig. 4). In addition, when vitrified phases exist, the pores in the ceramics are spherical (Cultrone et al., 2001). The observed pores in the studied ceramic samples are irregular (Figs. 1, 2).

The chemical and mineral composition of the raw clay, the firing temperature, and the gas atmosphere in the kiln determine the color of the ceramic. The investigated ceramic samples can be divided into two groups, depending on the color: beige with an orange tint (No. 57 and 71) and orange-brown – the remaining samples. The beige color is due to a higher content of calcite in raw clay (Kornilov, 2005), and the orange tint is a result of the proven hematite in both samples. Hematite was evidenced by PXRD, suggesting a content above 5% (1 - 1.5% hematite is sufficient to give a red color to the ceramic (Palanivel and Rajesh Kumar, 2009). The orange-brown color is characteristic of the remaining samples which were made of raw clay with a low carbonate content. For such ceramic, the color is controlled by the iron in the raw clay. In the original composition of the raw clay, iron can be present either as Fe^{2+} or as Fe^{3+} and can occupy both octahedral and tetrahedral positions (Janot and Delcroix, 1974). Both hematite and magnetite have been detected in the samples. Clay heat treatment leads to hematite formation after the clay mineral's structure breaks down. This process takes place at different temperatures according to various authors – for example, Cardiano et al. refer to a temperature of about 850°C (Cardiano et al., 2004), El Ouhabi et al. – a temperature of around 950°C (El Ouahabi et al., 2015). Regardless, the ceramic samples' firing temperatures did not exceed 807.9°C, indicating the absence of hematite crystallization. In this relation, hematite and magnetite can have the following origins: (i) raw minerals as a part of the raw clay, and (ii) newly-formed phases during ceramic firing because of goethite dehydroxylation (El Ouahabi et al., 2015). Dehydroxylation of goethite occurs at about 300 - 310°C, depending on impurities in natural goethite. Under oxidizing conditions, goethite dehydroxylation leads to the formation of hematite (Liu et al., 2023; Ponomar, 2018). Under reducing conditions, goethite transforms into magnetite at about 500°C (Ponomar, 2018). Knowing that the firing temperature of the samples exceeds 500°C, both origins are possible.

The examined ceramic samples have a fine porous structure (Figs. 1, 2, Table 1). The origin of pore-free spaces in fired ceramic could be due to the decomposition of organic (Goffer, 2007) and carbonate phases (Khitab et al., 2012). All studied samples contain calcite, and the calcite decomposition is not responsible for the pores' creation. Organic matter is a common impurity in clays (Chamley, 1989), and its decomposition temperature is in the 220-420°C range (Palanivel and Rajesh Kumar, 2009; Imman et al., 2021). According to the ceramic firing temperatures (above 500°C), the observed pores can be attributed to organic matter decomposition. In this regard, the detected organic phases by FTIR were of secondary origin. When the raw organic matter decomposed at oxidizing conditions, the empty pore spaces remained in the ceramic. When the organic decomposed in a reducing atmosphere with insufficient oxygen to oxidize the organic matter, the latter is charred and remains within the pores of the pottery as a black residue (Goffer, 2007). In the studied ceramic samples all pores were empty, indicating oxidizing conditions in the environment in the kiln, up to about 420°C. There is a possibility of a slightly reducing kiln environment after 420°C, allowing for magnetite crystallization to occur. The redox environment during the individual firing temperature ranges probably controls the magnetite/hematite ratio and the saturation of the ceramic color, respectively.

Ceramic often observes uneven coloring - black core and red rim. Such an effect appears when CO_2 from the decomposition of raw organic matter cannot leave the ceramic core, and oxygen cannot penetrate the core due to the ceramic's low porosity. As a result, a complete reduction of iron to magnetite occurs in the ceramic's core, giving it a black color. Avoiding this effect is accomplished by prolonging the firing time of the ceramics (Gredmaier et al., 2011; Barba et al., 1992). All the studied samples are uniform in color (Figs. 1, 2), which indicates that the production technology involved a long firing time.

4.3. *Some findings of ceramic quality and durability over time*

The examined bricks and tiles are well preserved (Figs. 1, 2), suggesting their quality and durability over time. The raw clay, the temperature, and the duration of the firing determine the durability and quality of the ceramic (Elert et al., 2003; Gredmaier et al., 2011). These parameters also control the degree of vitrification, where the vitrified (amorphous) phases increase the hardness of the ceramic but make it brittle and not resistant to weathering (Badica et al., 2022).

Clay, suitable for quality brick and tile production usually contains 20-30% Al_2O_3, 50-60% SiO_2, 1-5% CaO and 5-6% iron oxides (Khitab et al., 2021). It's assumed that the content of CaO should be low because when ceramic is fired above the decarbonation temperature, a large number of pores remain, and the prepared ceramic shrinks (Cultrone et al., 2001). In the examined samples, the content of Al_2O_3, SiO_2, and iron oxides falls within these limits. Only the content of CaO exceeds the indicated percentages (Table 2). The thermal analysis results show that a small part of the CaO is included in the calcite (Table 5), as only in samples No. 57 and No. 71 does this percentage exceed the required values, and in the remaining ones it is in an amount below one percent. Nevertheless, neither sample was fired at such high temperatures. All samples have a similar content of iron oxides, which

are known to determine not only the color of the ceramic but also its strength (Khitab et al., 2021). All samples contain quartz and feldspars, which preserve the shape of the ceramic and improve its mechanical properties (Khitab et al., 2021).

If the ceramic firing was at a higher temperature, above that of calcite decomposition, amorphous phases probably would not have formed, due to the specific chemical composition of the clay used. The oxides of alkali metals (sodium and potassium) are strong fluxes for ceramic. Their concentrations should be relatively low - between 3 and 5% (represented by oxides) to avoid melting during the ceramic production, as this would increase the volume of the vitrified phase. On the other hand, the alkaline earth metals - calcium and magnesium, extinguish melting caused by the alkalis providing solid-state crystallization of high-temperature phases (Aras and Kiliç, 2017). In the investigated ceramic samples, the amount of Na_2O + K_2O is from 4.31% (No. 71) to 6.73% (No. 20), and in the rest - it exceeds 5%. The sum of CaO and MgO is 14.82% and 22.10% (No. 71 and No. 57, respectively) and between 2.99% and 4.69% in the remaining samples (Table 2). Therefore, it could be accepted with a high probability that the DSC curve peaks in the 840°C - 1050°C temperature range (Fig. 6) show the formation of high-temperature phases by solid-state crystallization.

The uniform coloring of the investigated ceramic indicates not only the application of a long-time firing production technology, but also a high ceramic quality. The existence of a black core and red rim in fired ceramic leads to (i) a decrease in the compressive strength of the final product because the black core is less resistant to freezing, and (ii) swelling of the final product because the gases cannot leave the ceramic during firing, which also determines the low quality (Gredmaier et al., 2011).

5. CONCLUSION

The presented studies of archaeological ceramic (bricks and tiles) show the successful results from the combination of XRF, PXRD, FTIR, and thermal analysis to determine with great accuracy the mineral composition and type of the raw clay, the firing technology, and some findings of ceramic quality and durability over time.

The obtained results show:

(i) Similarity, with minor differences, between the mineral compositions of raw clays for all the samples:

- Raw clay minerals – illite, montmorillonite, glauconite, without clay minerals type 1:1.
- Raw accessory minerals – muscovite, chlorite (only for sample No. 141).
- Raw impurity minerals – quartz, potassium feldspar (microcline), plagioclase (albite), calcite, and amphibole (only for No. 71 and No. 141). The raw iron minerals could be +/- goethite, +/- magnetite, and +/- hematite.
- Raw organic phases.

(ii) All the studied samples were prepared from non-calcareous clay.

(iii) Two firing temperature ranges: 500°C - 700°C (No. 72 and No. 140) and 700°C - up to decarbonation temperature (all other samples). The 500°C - 700°C temperature range was found only for two Late Antique samples and could be accepted as an exception.

(iv) An oxidizing environment up to about 420°C with the possibility of a weakly reducing environment after this temperature.

(v) A prolonged firing process.

(vi) Raw clay with suitable chemical composition for making building ceramics, defined by an appropriate content of the main components - Al_2O_3, SiO_2, CaO, and iron oxides.

(vii) Frost (weathering) resistant, strong but not brittle (with improved mechanical properties) ceramic.

In conclusion, it can be accepted that:

(i) The raw clay used achieves the production of strong and time-resistant ceramic by applying adequate temperature, kiln atmosphere, and firing time.

(ii) The applied ceramic manufacturing technology was identical in the entire geographical area during the Roman and Late Antiquity periods.

These new results provide a possibility of restoration and conservation activities and a clear perspective for future investigation. They complement the known archaeological background by interpreting people's knowledge continuity from the Roman age to Late Antiquity and giving insight into their economic and cultural life, based on the ceramic experimental investigations. The identity in the qualities and features of the samples under research is a nice demonstration of continuity during the Transition as, nevertheless the hard changes, the vital ceramic production has survived in several local workshops.

Author Contributions: All authors contributed to the study conceptualization and design. Sample collection and description, B.D. and B.K; material preparation, data collection and analysis, B.K. and K.M. The first draft of the manuscript was written by all authors. All authors have read and agreed to the published version of the manuscript.

ACKNOWLEDGEMENTS

This work was funded by the National Science Fund of Bulgaria under grant KP-06-N39/9 (B.K., B.D).

REFERENCES

Aras, A. and Kiliç, S. (2017) The mineralogy and firing behavior of pottery clays of the Lake Van region, eastern Turkey. *Clay Minerals*, Vol. 52, No. 4, pp. 453 - 468. https://doi.org/10.1180/claymin.2017.052.4.04

Badica, P., Alexandru-Dinu, A., Grigoroscuta, M. A., Burdusel, M., Aldica, G. V., Sandu, V., Bartha, C., Polosan, S., Galatanu, A., Kuncser, V., Enculescu, M., Locovei, C., Porosnicu, I., Tiseanu, I., Ferbinteanu, M., Savulescu, I., Negru, M. and Batalu, N. D. (2022) Mud and burnt Roman bricks from Romula. *Scientific Reports*, Vol. 12, Article number: 15864. https://doi.org/10.1038/s41598-022-19427-7

Barba, A., Negre, F., Ortis, M. and Escardino, A. (1992). Oxidation of black core during the firing of ceramic ware – 3: influence of the thickness of the piece and the composition of the black core. *British Ceramic Transactions*, Vol. 91, pp. 36–46.

Bayazit, M., Işık, I., Issi, A. and Genç, E. (2014) Spectroscopic and thermal techniques for the characterization of the first millennium AD potteries from Kuriki - Turkey. *Ceramics International*, Vol. 40, No. 9, Part B, pp. 14769-14779. http://dx.doi.org/10.1016/j.ceramint.2014.06.068

Böke, H., Akkurt, S., İpekoğlu, B. and Uğurlu, E. (2006) Characteristics of brick used as aggregate in historic brick-lime mortars and plasters. *Cement and Concrete Research*, Vol. 36, No. 6, pp. 1115-1122. https://doi.org/10.1016/j.cemconres.2006.03.011

Boyanov, I. (2014) *Diskoduratere and the Emporia in Roman Thrace*. Sofia: Avalon Publishig.

Baziotis, I., Xydous, S., Manimanaki, S. and Liritzis, I. (2020) An integrated method for ceramic characterization: A case study from the newly excavated Kastrouli site (Late Helladic). *Journal of Cultural Heritage*, Vol. 42, pp. 274-279. https://doi.org/10.1016/j.culher.2019.08.003

Bratitsi, M., Liritzis, I., Vafiadou, A., Xanthopoulou, V., Palamara, E., Iliopoulos, Y. and Zacharias, N. (2018) Critical assessment of chromatic index in archaeological ceramics by Munsell and RGB: Novel contribution to characterization and provenance studies. *Mediterranean Archaeology and Archaeometry*, Vol. 18, No. 2, pp. 175-212. https://doi.org/10.5281/zenodo.1297163

Caccamo, M. T., Mavilia, G., Mavilia, L., Lombardo, D. and Magazù, S. (2020) Self-Assembly Processes in hydrated montmorillonite by FTIR investigations. *Materials*, Vol. 13, No. 5, p. 1100. https://doi.org/10.3390/ma13051100

Cardiano, P., Ioppolo, S., De Stefano, Co., Pettignano, A., Sergi, S. and Piraino, P. (2004) Study and characterization of the ancient bricks of monastery of "San Filippo di Fragalà" in Frazzanò (Sicily). *Analytica Chimica Acta*, Vol. 519, No. 1, pp. 103-111. https://doi.org/10.1016/j.aca.2004.05.042

Carretero, M. I., Dondi, M., Fabbri, B. and Raimondo, M. (2002) The influence of shaping and firing technology on ceramic properties of calcareous and non-calcareous illitic–chloritic clays. *Applied Clay Science*, Vol. 20, No. 6, pp. 301-306. https://doi.org/10.1016/S0169-1317(01)00076-X

Chamley, H. (1989) *Clay Sedimentology*. Berlin Heidelberg: Springer-Verlag. https://doi.org/10.1007/978-3-642-85916-8

Chukanov, N. V. (2014) *Infrared spectra of mineral species: Extended library*. Springer Geochemistry/Mineralogy, Dordrecht Heidelberg New York London: Springer.

Chukanov, N. V. and Chervonnyi, A. D. (2016) *Infrared Spectroscopy of Minerals and Related Compounds*. New York Dordrecht London: Springer. https://doi.org/10.1007/978-3-319-25349-7

Cultrone, G., Rodriguez-Navarro, C., Sebastian, E., Cazalla, O. and De Le Torre, M. J. (2001) Carbonate and silicate phase reactions during ceramic firing. *European Journal of Mineralogy*, Vol. 13 No. 3, pp. 621-634. https://doi.org/10.1127/0935-1221/2001/0013-0621

Drebushchak, V., Mylnikova, L., Drebushchak, T. and Boldyrev, V. V. (2005) The investigation of ancient pottery. *Journal of Thermal Analysis and Calorimetry*, Vol. 82, pp. 617–626. https://doi.org/10.1007/s10973-005-0942-9

Dumanov, B. (2005) Rescue archaeological excavations of site N 13A near the village of Malko Tranovo, Chirpan municipality. *Archaeological Discoveries and Excavation in 2004 г. XLIV National Archaeological Conference*. Sofia: Bulgarian Academy of Sciences. pp. 243 – 244.

El Ouahabi, M., Daoudi, L., Hatert, F. and Fagel, N. (2015) Modified mineral phases during clay ceramic firing. *Clays and Clay Minerals*, Vol. 63, pp. 404–413. https://doi.org/10.1346/CCMN.2015.0630506

Elert, K., Cultrone, G., Navarro, C. R. and Pardo, E. S. (2003). Durability of bricks used in the conservation of historic buildings — influence of composition and microstructure. *Journal of Cultural Heritage*, Vol. 4, No. 2, pp. 91-99. https://doi.org/10.1016/S1296-2074(03)00020-7

Emami, M., Sakali, Y., Pritzel, Ch. and Trettin, R. (2016) Deep inside the ceramic texture: A microscopic–chemical approach to the phase transition via partial-sintering processes in ancient ceramic matrices. *Journal of Microscopy and Ultra Structure*, Vol. 4 No. 1, pp. 11-19. http://dx.doi.org/10.1016/j.jmau.2015.08.003

Földvári, M. (2007) *Handbook of the thermogravimetric system of minerals and its use in geological practice*. Occasional Papers of the Geological Institute of Hungary. Budapest. https://doi.org/10.1556/ceugeol.56.2013.4.6

Goffer, Z. (2007) *Archaeological chemistry. Chemical analysis: A series of monographs on analytical chemistry and its applications.* 2nd ed. Hoboken, New Jersey: Wiley & Sons, Inc.

Gonidanga, B. S., Njoya, D., Lecomte-Nana, G. and Njopwouo, D. (2019) Phase transformation, technological properties and microstructure of fired products based on clay-dolomite mixtures. *Journal of Materials Science and Chemical Engineering*, Vol. 7, No. 11. https://doi.org/10.4236/msce.2019.711001

Gredmaier, L., Banks, C. J. and Pearce, R. B. (2011) Calcium and sulphur distribution in fired clay brick in the presence of a black reduction core using micro X-ray fluorescence mapping. *Construction and Building Materials*, Vol. 25, No. 12, pp. 4477-4486. https://doi.org/10.1016/j.conbuildmat.2011.03.054

Hamilton, A. and Hall Ch. (2012) A review of rehydroxylation in fired-clay ceramics. *Journal of the American Ceramic Society*, Vol. 95, No. 9. https://doi.org/10.1111/j.1551-2916.2012.05298.x

Hatakeyama, T. and Liu, Zk. (1998) *Handbook of thermal analysis*. Sussex, England: John Wiley & Sons Ltd.

Imman, S., Khongchamnan, P., Wanmolee, W., Laosiripojana, N., Kreetachat, T., Akulthaew, Ch., Chokejaroenrat, Ch. and Suriyachai, N. (2021) Fractionation and characterization of lignin from sugarcane bagasse using a sulfuric acid catalyzed solvothermal process. *RSC Advances*, Vol. 11, pp. 26773 https://doi.org/10.1039/D1RA03237B

Ion, R-M, Ion, M-L., Fierascu, R. C., Serban, S., Dumitriu, I., Radovici, C., Bauman, I., Cosulet, S. and Niculescu, V. (2010) Thermal analysis of Romanian ancient ceramics. *Journal of Thermal Analysis and Calorimetry*, Vol. 102, pp. 393–398. https://doi.org/10.1007/s10973-009-0226-x

Janot, Ch. and Delcroix, P. (1974) Mössbauer study of ancient french ceramics. *Journal de Physique Colloques*, Vol. 35, pp. C6-557-C6-561.

Jozanikohan, G. and Abarghooei, M. N. (2022) The Fourier transform infrared spectroscopy (FTIR) analysis for the clay mineralogy studies in a clastic reservoir. *Journal of Petroleum Exploration and Production Technology*, Vol. 12, pp. 2093–2106. https://doi.org/10.1007/s13202-021-01449-y

Khalifa, A. Z., Pontikes, Y., Elsen, J. and Cizer, Ö. (2019) Comparing the reactivity of different natural clays under thermal and alkali activation. *RILEM Technical Letters*, Vol. 4, pp. 74-80. https://doi.org/10.21809/rilemtechlett.2019.85

Khitab, A., Riaz, M. S., Jalil, A., Khan, R. B. N., Anwar, W., Khan, R. A., Arshad, M. T., Kirgiz, M. S., Tariq, Z. and Tayyab, S. (2021) Manufacturing of clayey bricks by synergistic use of waste brick and ceramic powders as partial replacement of clay. *Sustainability-*, Vol. 13, No. 18, pp. 10214. https://doi.org/10.3390/su131810214

Kılıç, N. Ç., Kılıç, S. and Akgül, H. Ç. (2017) An archaeometric study of provenance and firing technology of halaf pottery from Tilkitepe (Eastern Turkey). *Mediterranean Archaeology and Archaeometry*, Vol. 17, No. 2, pp. 35-48. https://doi.org/10.5281/zenodo.581718

Kornilov, A. V. (2005) Reasons for the different effects of calcareous clays on strength properties of ceramics. *Glass and Ceramics*, Vol. 62, pp. 391–393. https://doi.org/10.1007/s10717-006-0017-9

Kostova, B., Dumanov, B., Stoyanov, V. and Shivachev, B. (2023). Thermal and phase analysis of Roman and Late Antiquity mortars from Bulgarian archaeological sites. *Journal of Thermal Analysis and Calorimetry*, Vol. 148, pp. 1543–1555. https://doi.org/10.1007/s10973-022-11493-3

Kotryová, B., Ondruška, J., Štubňa, I. and Bačík, P. (2016) Thermoanalytical investigation of ancient pottery. *AIP Conference Proceedings*, 1752, pp. 040016. https://doi.org/10.1063/1.4955247

Krapukaityte, A., Tautkus, S., Kareiva, A. and Zalieckiene, E. (2008) Thermal analysis - A powerful tool for the characterization of pottery. *Chemija*, Vol. 19, pp. 4-8.

Laufek, F., Hanusová, I., Svoboda, J., Vašíček, R., Najser, J., Koubová, M., Čurda, M., Pticen, F., Vaculíková, L., Sun, H. and Mašín, D. (2021) Mineralogical, geochemical and geotechnical study of BCV 2017 Bentonite - the initial state and the state following thermal treatment at 200°C. *Minerals*, Vol. 11, No. 8, pp. 871. https://doi.org/10.3390/min11080871

Lee, W. E., Souza, G. P., McConville, C.J., Tarvornpanich, T. and Iqbal, Y. (2008) Mullite formation in clays and clay-derived vitreous ceramics. *Journal of the European Ceramic Society*, Vol. 28, No. 2, pp. 465-471. https://doi.org/10.1016/j.jeurceramsoc.2007.03.009

Liu, H., Chen, T., Zou, X., Qing, C. and Frost, R. L. (2013) Thermal treatment of natural goethite: Thermal transformation and physical properties. *Thermochimica Acta*, Vol. 568, pp. 115-121. https://doi.org/10.1016/j.tca.2013.06.027

Marsh, A., Heath, A., Patureau, P., Evernden, M. and Walker, P. (2018) Alkali activation behavior of un-calcined montmorillonite and illite clay minerals. *Applied Clay Science*, Vol. 166, pp. 250-261. https://doi.org/10.1016/j.clay.2018.09.011

Meyers, K. S. and Speyer, R. F. (2003) Thermal analysis of clays. In: *Brown ME, Gallacher PK, editors. Handbook of Thermal analysis and Calorimetry. 2. Applications to inorganic and miscellaneous materials*. Amsterdam: Elsevier; 2003. pp 268-289.

Moropoulou, A., Bakolas, A. and Bisbikou, K. (1995) Characterization of ancient, byzantine and later historic mortars by thermal and X-ray diffraction techniques. *Thermochimica Acta*, Vol. 269–270, pp. 779-795. https://doi.org/10.1016/0040-6031(95)02571-5

Muller, F., Drits, V., Plançon, A. and Robert, J-L. (2000) Structural Transformation of 2:1 dioctahedral layer silicates during dehydroxylation-rehydroxylation reactions. *Clays and Clay Minerals*, Vol. 48, pp. 572–585. https://doi.org/10.1346/CCMN.2000.0480510

Neff, H. (1993) Theory, sampling, and analytical techniques in the archaeological study of prehistoric ceramics. *American Antiquity*, Vol. 58, No. 1, pp. 23-44. https://doi.org/10.2307/281452

Omar, S. (2022) Characterization of the Ottoman ceramic tiles in the façade of Mustafa Sinan's Sapil (Cairo, Egypt). *Scientific culture*, Vol. 8, No. 2, pp. 1-15. DOI: 10.5281/zenodo.6323156

Palanivel, R. and Rajesh Kumar, U. (2009) Thermal and spectroscopic analysis of ancient potteries. *Romanian Journal of Physics*, Vol. 56, No. 1-2, pp. 195-208.

Papadopoulou, D. N., Lalia-Kantouri, M., Kantiranis, N. and Stratis, J. A. (2006) Thermal and mineralogical contribution to the ancient ceramics and natural clays characterization. *Journal of Thermal Analysis and Calorim*etry, Vol. 84, pp. 39–45. https://doi.org/10.1007/s10973-005-7173-y PDF (Powder Diffraction File). (2001) ICDD, Newtown Square, PA.

Peacock, D. P. S. (1970) The scientific analysis of ancient ceramics: a review. *World Archaeology*, Vol. 1, No. 3, pp. 375-389.

Pei, Z., Lin, M., Liu, Y. and Lei, S. (2018) Dissolution behaviors of trace muscovite during pressure leaching of hydrothermal vein quartz using H_2SO_4 and NH_4Cl as leaching agents. *Minerals*, Vol. 8, No. 2, pp. 60. https://doi.org/10.3390/min8020060

Pérez-Monserrat, E., Maritan, L., Garbin, E. and Cultrone, G. (2021) Production technologies of ancient bricks from Padua, Italy: changing colors and resistance over time. *Minerals*, Vol. 11, No. 7, pp. 744. https://doi.org/10.3390/min11070744

Ponomar, V. P. (2018) Thermomagnetic properties of the goethite transformation during high-temperature treatment. *Minerals Engineering*, Vol. 127, pp. 143-152. https://doi.org/10.1016/j.mineng.2018.08.016

Rao, H., Yang, Y., Hu, X., Yu, J. and Jiang, H. (2017) Identification of an ancient birch bark quiver from a Tang Dynasty (A.D. 618–907) tomb in Xinjiang, Northwest China. *Economic Botany*, Vol. 71, pp. 32–44. https://doi.org/10.1007/s12231-017-9369-z

Ravisankar, R., Kiruba, S., Eswaran, P., Senthilkumar, G. and Chandrasekaran, A. (2010) Mineralogical Characterization Studies of Ancient Potteries of Tamilnadu, India by FT-IR Spectroscopic Technique. *E-Journal of Chemistry*, Vol. 7, No. S1, pp. S185-S190. https://doi.org/10.1155/2010/643218

Silva, A., Wenk, H. R. and Monteiro, P. J. M. (2005) Comparative investigation of mortars from Roman Colosseum and cistern. *Thermochimica Acta*, Vol. 438, No. 1–2, pp. 35-40. https://doi.org/10.1016/j.tca.2005.03.003

Singha, M. and Singh, L. (2016) Vibrational spectroscopic study of muscovite and biotite layered phyllosilicates. Indian *Journal of Pure and Applied Physics*, Vol. 54, pp.116-122.

Stanienda, K. J. (2016) Carbonate phases rich in magnesium in the Triassic limestones of the eastern part of the Germanic Basin. *Carbonates Evaporites*. Vol. 31, pp. 387–405. https://doi.org/10.1007/s13146-016-0297-2

Theodosoglou, E., Koroneos, A., Soldatos, T., Zorba, T. and Paraskevopoulos, K. M. (2010) Comparative Fourier transform infrared and X-Ray powder diffraction analysis of naturally occurred K-feldspars *Bulletin of the Geological Society of Greece*, Vol. 43, No. 5, pp. 2752–2761. https://doi.org/10.12681/bgsg.11681

Trindade, M. J,. Dias, M. I., Coroado, J. and Rocha, F. (2009) Mineralogical transformations of calcareous rich clays with firing: A comparative study between calcite and dolomite rich clays from Algarve, Portugal. *Applied Clay Science*, Vol. 42, No. 3–4, pp. 345-35. https://doi.org/10.1016/j.clay.2008.02.008

Velosa, A.L., Coroado, J., Veiga, M. R. and Rocha, F. (2007) Characterisation of roman mortars from Conímbriga with respect to their repair. *Materials Characterization*, Vol. 58, No. 11–12, pp. 1208-1216. https://doi.org/10.1016/j.matchar.2007.06.017

Vlase, D., Rogozea, O., Moşoiu, C., Vlase, G., Lazău, R. and Vlase, T. (2019) Thermoanalytical investigations of some ceramics dated from the Neolithic period, discovered at Oxenbrickel, Sânandrei, Romania. *Journal of Thermal Analysis and Calorimetry*, Vol. 138, pp. 2145–2157. https://doi.org/10.1007/s10973-019-08767-8

Wendel, M. (2001) Der Fundplatz Karasura. In: M. Wendel (Hrsg.) *Untersuchungen zur Geschichte und Kultur des alten Thrakien I. 15 Jahre Ausgrabungen in Karasura*. Internationales Symposium Čirpan/Bulgarien 1996. Weissbach: Beier & Beran, pp. 5-32.

Xanthopoulou, V., Iliopoulos, I. and Liritzis, I. (2020) Characterization techniques of clays for the archaeometric study of ancient ceramics: A review. *Scientific culture*, Vol. 6, No. 2, pp. 73-86. https://doi.org/10.5281/zenodo.3724849

Yan, B., Liu, S., Chastain, M. L., Yang, Sh. and Chen, J. (2021) A new FTIR method for estimating the firing temperature of ceramic bronze-casting moulds from early China. *Scientific Reports*, Vol. 11, Article number: 3316. https://doi.org/10.1038/s41598-021-82806-z